IEEE Access
Multidisciplinary ⋮ Rapid Review ⋮ Open Access Journal

Received 14 May 2023, accepted 23 May 2023, date of publication 29 May 2023, date of current version 9 June 2023.

*Digital Object Identifier 10.1109/ACCESS.2023.3280825*

RESEARCH ARTICLE

# Design of a Controller for Grid Forming Inverter-Based Power Generation Systems

**MD. MINARUL ISLAM[1], (Member, IEEE), KASHEM M. MUTTAQI[2], (Fellow, IEEE), DANNY SUTANTO[2], (Life Senior Member, IEEE), MD. MOKTADIR RAHMAN[3], AND OSCAR ALONSO[4]**

[1]Department of Electrical and Electronic Engineering, Faculty of Engineering and Technology, University of Dhaka, Dhaka 1000, Bangladesh
[2]Australian Power and Energy Research Institute (APERI), School of Electrical, Computer and Telecommunications Engineering, Faculty of Engineering and Information Sciences, University of Wollongong, Wollongong, NSW 2522, Australia
[3]Essential Energy, Port Macquarie, NSW 2444, Australia
[4]SiG coop, 31013 Artica, Spain

Corresponding author: Md. Minarul Islam (mmislam-eee@du.ac.bd)

This work was supported in part by the University of Dhaka, in part by the Australian Research Council (ARC), in part by the University of Wollongong, and in part by Ingeteam Australia Pty, Ltd.

**ABSTRACT** Recently the grid-following inverter-based power generation systems (IBPGSs) dominate over synchronous generators (SGs) in load sharing in some areas of power grids in many countries worldwide. The trend of increasing penetration of IBPGSs to grid results in decreasing number of SGs in operation. This can result in a slowly decreasing system inertia which results in fast dynamics during transient conditions, that may lead to failures of phase-locked loops (PLLs), which are widely used in grid-following IBPGSs. Consequently, the grid-following IBPGS-dominated grids are facing stability issues in their operations. To support these grid-following IBPGSs for their stable operations, a stable grid-forming IBPGS is required that can operate as SGs. In this paper, a grid-forming controller is designed for IBPGSs that can enable IBPGSs to mimic SGs and work as grid-forming inverters that operate like SGs to maintain the grid dynamics suitable for the stable operation of the IBPGSs. For this purpose, a detailed mathematical model of the SG and its associated controller has been used with the proposed grid-forming controller. From the steady-state and transient dynamics, a mathematical relationship between the inertia support from the grid-forming controller and an SG has been developed to control the inverter in the grid-forming IBPGS. The performance of the grid-forming IBPGS during steady-state and transients due to load change, fault, and grid-isolation has been compared with the SG. The simulation results have validated the effectiveness of the proposed controller and grid-forming IBPGSs to help control the voltage and frequency of the IBPGS-dominated power systems.

**INDEX TERMS** Controller design, grid forming inverter, grid inertia, virtual inertia, steady-state analysis, transient analysis.

## I. INTRODUCTION

To reduce $CO_2$ emissions, the power systems in many countries worldwide are strongly encouraged to increase the penetration of renewable energy system (RES)-based distributed generations (DGs) [2], [3]. However, with the increasing penetration of RES-based DGs, such as solar photovoltaics (PVs), wind turbines, and battery energy storage systems (BESSs), the power systems in many countries have already observed instances of surplus instantaneous power generations relative to demands. It is expected that as the penetration increases further, the surplus instantaneous power generation could be three to five times larger than the annual average power generation [1]. The situation will become worse as it is envisioned in some European countries, that the RES-based DGs will supply 100% of the demand by 2025 [1]. Furthermore, the high penetration of RES-based DGs will replace a considerable number of conventional SGs, which will affect the current paradigm of the power system operation and control.

The associate editor coordinating the review of this manuscript and approving it for publication was Inam Nutkani.

Most of these RES-based DGs are IBPGSs which don't possess the attributes of SGs. Hence, the grid operators with fewer SGs and more IBPGSs are experiencing unprecedented challenges, such as reduced system inertia [4] that can lead to the failure in the operation of PLLs [5], [6], [7], increased rate of change of frequency (ROCOF) [8], [9], the increasing need for the disturbance ride-through capability [10], [11], [12], the activation of frequency relays, which may cause under-frequency load shedding, [13], [14], required contingency frequency control during islanding operations [1], [4] and the system restoration capability [1]. The grid operators in Ireland and Britain have already reported that the grid operation challenges during any disturbance will be significantly worsened when the load sharing by the IBPGSs exceeds more than 65% of system demands [1], [4]. The challenges caused by the high penetration level of IBPGSs are system-specific and depend on (i) the number of SGs in operation in the system, (ii) their locations, (iii) their capacities compared to the integrated IBPGS generation levels, (iv) the magnitudes of the largest reliable contingency power plants, (v) the strength of IBPGS's controllers, and (vi) the availability of interconnections with neighboring power systems. How these new challenges with large penetration of IBPGSs will be tackled is still being investigated by all grid operators.

There are two operation modes of IBPGSs in grid-connected or islanded systems, either in the grid-following mode or in the grid-forming mode. The majority of IBPGSs currently operating in any grid worldwide is the grid-following one [1]. These grid-following IBPGSs consist of fast-controlled power electronic converters and require a stable grid for their continuous operation. In a stable grid dominated by a large presence of SGs with their slow inherent electromechanical characteristics, the overall system electromechanical dynamics change slowly. Therefore, the grid-following IBPGSs can easily track the grid voltage accurately and can feed current to the grid at the correct phase angle. However, with the increasing penetration of grid-following IBPGSs, the number of SGs decreases, hence the total system inertia decreases. Therefore, the effect of the electromechanical dynamics lessens while the faster electrical dynamics dominate [1], [4]. Hence, the grid-following IBPGSs may potentially lose synchronization [1], [4], [5], [6], [7] and may fail to be remained connected with the grid due to a small disturbance, which may lead to grid instability. To maintain grid stability, grid feeding from grid-following IBPGSs has been limited to many grids worldwide which may impede further growth of the grid-following IBPGSs in the long run [1]. To support an IBPGS-rich grid, some grid operators have set the requirements of must-run SG or synchronous condensers (SCs). However, the use of SCs is an expensive choice.

Recently, the grid-forming IBPGS has attracted the attention of researchers, which requires no must-run SGs or SCs to maintain grid stability during any grid conditions. This grid-forming IBPGS with its voltage and frequency support capability either in grid-connected or islanded mode of operation has generally been defined as grid-forming inverters (GFMIs). Like SGs, these GFMIs can maintain a slow grid dynamic for the stable operation of the grid-following IBPGSs, which is only possible if the GFMIs possess the following functionalities:

1. Under normal grid-connected mode, it should behave as an ac voltage source operating within its physical constraints.
2. Under islanding mode, it should help to form the grid autonomously.
3. Under transient mode during faults or system changes, it should behave as an ac voltage source, as long as its constraints are not violated. However, if its limits are violated, its operation may temporarily fall into a specific regime to maintain its limits.
4. Under blackout or brownout mode, it should support the grid restoration process with the help of energy storage in the system.

Several control techniques have been proposed for the IBPGSs in the literature to meet the functionalities of the GFMIs mentioned above, such as (i) frequency-droop control [15], [16], (ii) angle-droop control [17], [18], (iii) virtual synchronous machines (VSMs) control [19], [20], [21], [22], and (iv) dispatchable virtual oscillator control (dVOC) [23]. As most of these control techniques for IBPGSs are based on the load-frequency imbalance, they maintain the fundamental operation of the system. However, due to the reduced inertia, the borderline between the primary and the secondary frequency control could shift with the faster system dynamics. Although the IBPGS controllers are capable of fast response to any contingency in the system [4], they are usually designed and operated at a reduced bandwidth to (i) ensure system stability [24], and (ii) ensure that the system frequency or the voltage phase-angle does not vary too fast so that the PLLs used in IBPGSs can accurately track the system dynamics for frequency support.

Among the grid-forming IBPGSs, the VSMs and synchronverters (SVs) [19], [20], [21], [22], [25] have been designed to inherit the attributes of an SG under a wide range of operating conditions. Some of the controllers of the SVs have been designed with trigonometric functions [25]. Therefore, although these controllers are appropriate for time-domain simulation, their small signal stability response analyses in the frequency domain are complex and complicated.

It is worth mentioning here, that the SGs maintain the grid voltage and frequency when the load sharing of the IBPGSs to SGs is low [1], [4]. In that low-load sharing ratio, controllers of the grid-following and grid-forming IBPGSs (e.g., VSMs, SVs) were designed and developed to have faster voltage support to grid disturbance that results in excluding many elements of the SG-controller [19], [20], [21], [22], [25], [26]. Some of the VSM controllers were modeled with very low or zero inertia [25], [26], [34], [35], [36]. Therefore, the dynamics of the existing IBPGSs (both GFMIs and grid-following) are relatively faster than the SGs. Consequently, there occurs dynamic interaction among the IBPGSs and the

SGs with the grids that can cause oscillation in a wide range of frequencies [27]. Based on the above-reported literature, it is important to highlight here that to avoid dynamic interaction and oscillation among the IBPGSs and SGs and to support the uninterrupted operation of the grid-following IBPGSs, the GFMIs should be designed to have similar attributes of SGs. This may help avoid modification of the controllers of the existing grid-following IBPGSs to cope with fast dynamics in a reduced or low inertia grid.

This paper proposes a new controller for the grid-forming IBPGS to control system dynamics suitable for the stable operation of the grid-following IBPGSs. The controller has been designed based on a detailed electromagnetic and electromechanical model of an SG and its associated controllers, which include a model of the turbine, a speed-droop controller with its speed relay, an exciter, an automatic voltage regulator (AVR), and a power system stabilizer (PSS). Therefore, the key difference between the existing VSM/SV system and the proposed system in the paper is in their modeling. To slow down the grid dynamics which is beneficial for the stable operation of existing grid-following IBPGSs, all the peripheral controller parts of an SG have been used in the controller of the GFMI. The proposed controller for the grid-forming IBPGS has been validated through MATLAB simulation either in grid-connection or grid-isolation modes, and its performance in terms of inertia support and maintaining system dynamics has been compared with those of an SG. The comparisons presented in this paper show that the proposed controller can closely follow the performance of an SG. Therefore, it is expected that the proposed controller for the GFMI will provide inertia support to the power system and will form a stable grid similar to what an SG does for the stable and uninterruptible operation of the grid-following IBPGSs. In this paper, grid-following and grid-forming IBPGSs have been synonymously used with grid-following inverters (GFLIs) and GFMIs, respectively.

## II. LOW INERTIA EFFECT ON THE OPERATION OF GRID-FOLLOWING INVERTER

A grid-following inverter (GFLI) requires a strong grid to be synchronized for its stable and uninterruptible operation. The synchronous reference frame-PLL (SRF-PLL) is widely used in tracking the phase angle and fundamental frequency of the grid voltage at the PCC. Therefore, the operation of the GFLI undoubtedly depends on the performance of the SRF-PLL. However, the increasing penetration of GFLIs and the reduction of SGs connected to the grid results in decreasing mechanical inertia, short-circuit ratio (SCR), strength, and frequency-stability margin of the grid. As a result, the grid behaves as a weak grid [28] and experiences a rapid ROCOF during any disturbance. The authors in [7] reported a fast ROCOF of 10 Hz/s during a short-circuit fault in the Bonaire Island weak grid. The SRF-PLL performs poorly in a weak grid during a high ROCOF situation which affects the operation of the GFLI.

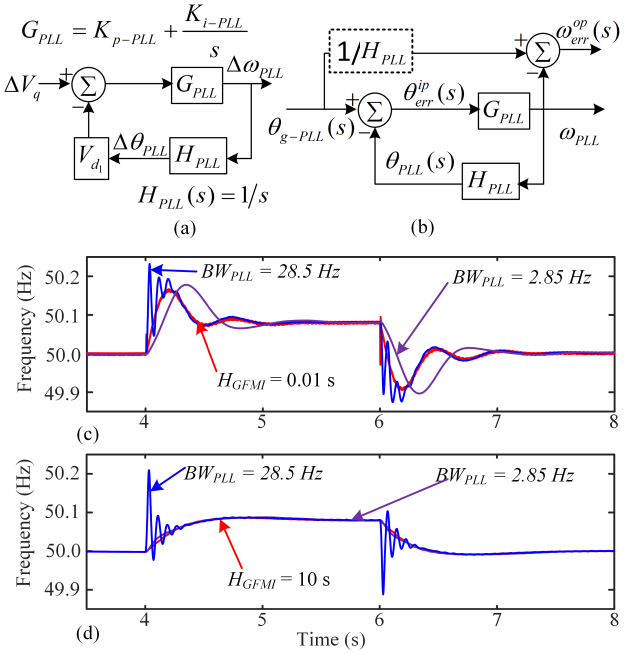


**FIGURE 1.** (a) Small signal closed-loop transfer function diagram of a PLL, (b) definition of a feedback control system with input and output error, (c) frequency tracking error by the PLL during fast dynamics, (d) frequency tracking error by the PLL during slow dynamics.

The performance of the SRF-PLL depends on its designed parameter, especially its bandwidth. Although the bandwidth of the SRF-PLL can be designed high to track a high ROCOF, it is kept lower in a weak grid to filter out residue harmonics in the PCC voltage and to limit spurious harmonic currents [29]. The SRF-PLL with a lower bandwidth possesses a characteristic of slower dynamic which helps the stable operation of the GFLI. On the contrary, the SRF-PLL with higher bandwidth may trigger harmonic instability of the GFLI [6]. Therefore, it has been a common trend worldwide to design the SRF-PLL with lower bandwidth to ensure the stable operation of the GFLI.

Fig. 1(a) [7] shows a general structure of an SRF-PLL.

The voltage relationship between the *dq0*- and the *abc*-reference phases can be expressed by (1) and (2).

$$V_q = V_m \sin(\theta_{g-PLL} - \theta_{PLL}) \tag{1}$$

$$V_d = V_m \cos(\theta_{g-PLL} - \theta_{PLL}) \tag{2}$$

If the $a$-axis in SRF is aligned with the $q$-axis in the *dq0*-frame, i.e., $\Delta\theta = \theta_{g-PLL} - \theta_{PLL} = 0$, then $V_q = 0$ and $V_d = V_m$. Now normalizing in per unit system $V_q = 0$ and $V_d = V_m$, equations (1) and (2) change to the equations in (3) and (4) respectively,

$$V_q = \sin(\theta_{g-PLL} - \theta_{PLL}) \tag{3}$$

$$V_d = \cos(\theta_{g-PLL} - \theta_{PLL}) \tag{4}$$

Now for small perturbation, (3) and (4) can be linearized around the steady-state operating point $\Delta\theta_0 = 0$ and

expressed by (5) and (6), respectively.

$$\Delta V_q = \cos(\Delta\theta_0)\Delta\theta \tag{5}$$

$$\Delta V_d = -\sin(\Delta\theta_0)\Delta\theta \tag{6}$$

Therefore, for a small perturbation around the steady-state operating point $\Delta\theta_0 = 0$, $\Delta V_q = \Delta\theta$ and $\Delta V_d = 0$. The change in the output frequency of the SRF-PLL can be expressed by (7)-(8) [7].

$$\Delta\omega_{PLL}(s) = \frac{G_{PLL}(s)}{1 + G_{PLL}(s)\,H_{PLL}(s)}\Delta\theta(s) \tag{7}$$

$$\Delta\theta_{PLL}(s) = H_{PLL}(s)\Delta\omega_{PLL}(s) \tag{8}$$

From Fig. 1(b), the phase angle error to the PLL is expressed in (9).

$$\theta^{ip}_{err}(s) = \theta_{g-PLL}(s) - \theta_{PLL}(s) \tag{9}$$

$$\omega^{op}_{err}(s) = \frac{\theta_{g-PLL}(s)}{H_{PLL}(s)} - \omega_{PLL}(s) \tag{10}$$

$$\omega^{op}_{err}(s) = \frac{\theta^{ip}_{err}(s)}{H_{PLL}(s)} \tag{11}$$

Equation (9) can be represented as in (12)

$$\theta^{ip}_{err}(s) = \frac{\theta_{g-PLL}(s)}{1 + G_{PLL}(s)\,H_{PLL}(s)} \tag{12}$$

During disturbances in the power system, the system frequency $f(t)$ deviation and the corresponding phase angle deviation can be expressed by (13) and (14), respectively [7].

$$\omega_{g-PLL}(t) = 2\pi \times ROCOF \times t \tag{13}$$

$$\theta_{g-PLL}(t) = \omega_{g-PLL}(t)\,t = 2\pi \times ROCOF \times t^2 \tag{14}$$

Using the final value theorem, the steady-state phase angle error can be calculated as follows:

$$\lim_{s\to 0} s\theta^{ip}_{err}(s) = s\frac{\theta_{g-PLL}(s)}{1 + G_{PLL}(s)\,H_{PLL}(s)} \tag{15}$$

$$\lim_{s\to 0} s\theta^{ip}_{err}(s) = s\frac{4\pi \times ROCOF}{s^2 + K_{p-PLL}s + K_{i-PLL}} = \frac{4\pi \times ROCOF}{K_{i-PLL}} \tag{16}$$

Equation (16) shows that the steady-state phase angle error is a function of ROCOF and $K_{i-PLL}$. For a larger ROCOF in a low inertia system, the PLL will have a larger phase angle error. However, the phase angle error can be reduced using a larger value of $K_{i-PLL}$. Here is the contradiction of designing the PLL bandwidth, because the larger the value of $K_{i-PLL}$ means the larger the bandwidth of the PLL, which may cause instability of GFLI.

To check the performance of the SRF-PLL, a fast and slow dynamic corresponding to system inertia of 0.01 s and 10 s, respectively, were simulated by creating frequency events at t = 4 s in Fig. 8. Figs. 1(c) and 1(d) show that the ROCOF of the system with the inertia of 0.01 s is faster than the ROCOF of the system with the inertia of 10 s. The bandwidths (BWs) of the SRF-PLL were designed as 28.5 Hz (high $BW_{PLL}$) and 2.85 Hz (low $BW_{PLL}$).

Fig. 1(c) shows that with the low $BW_{PLL}$, the frequency tracking error is high, and the SRF-PLL takes more than 1 s to exactly follow the system frequency. However, the SRF-PLL with high $BW_{PLL}$ closely tracks the system frequency with some initial oscillations as shown in Fig. 1(c).

Fig. 1(d) shows that with the low $BW_{PLL}$, the SRF-PLL exactly follows the system frequency. The SRF-PLL with high $BW_{PLL}$ also tracks the system frequency with a similar initial oscillation as shown in Fig. 1(d). The SRF-PLL takes less than 300 ms in both slow and fast dynamics to exactly track the ROCOF in the system.

From the above analysis, it can be concluded that the GFMIs which will provide similar support to an SG, will be very crucial for the stable and uninterruptible operation of a power system dominated by GFLIs in load sharing in the future power grid.

## III. PROPOSED CONTROLLER FOR GRID-FORMING INVERTER

The proposed GFMI controller has been described in detail in this section. All the components of a traditional SG are included to develop the controller for the GFMI based on the hypothesis that as the SG is a well-known grid-forming system, this GFMI will also be a grid-forming system to support grid-following IBPGSs to form a stable grid. The design of the proposed GFMI, in Fig. 2, includes two parts: (1) the electrical part and (2) the controller part. The controller part communicates with the electrical circuit part via $v_{oabc}$, $i_{fabc}$, and $g_{abc}$ signals. The current $i_{fabc}$ and the voltage $v_{oabc}$ are measured using current and voltage sensors, respectively, and passed through the low pass filter (LPF) for conditioning. The circuits of these sensors, LPF, reference frame transformation (abc/dq0), and sinusoidal pulse-width modulation (SPWM) are well documented in the literature [30], [31].

### A. ELECTRICAL PART

The design of the electrical circuit part of the GFMI, shown in Fig. 2(a), includes the design of a solar PV source, a dc-dc boost converter, a dc-link formed by a dc side capacitor $C_{dc}$, a three-phase inverter, a BESS, a bidirectional dc-dc converter, and an LC filter. The PV array and the BESS are connected to the dc-link through a boost converter and a bidirectional dc-dc converter, respectively. The BESS has been designed as an equivalent kinetic energy reserve to the rotor of an SG since the GFMI behaves like an SG. In the LCL filter, the LC part includes the design of an inductance $L_f$, a capacitance $C_f$, a resistance $R_f$, and a damping resistance $R_d$, to reduce the ripples of the voltage and current outputs from the GFMI, and to suppress the total harmonic distortion (THD) below 5% specified by the standards [32]. On the grid side, the inductance $L_l$ and the resistance $R_l$, are the equivalent inductances and resistances of the step-up transformer and the connecting line as well as the Thevenin equivalent inductance and resistance of the grid.

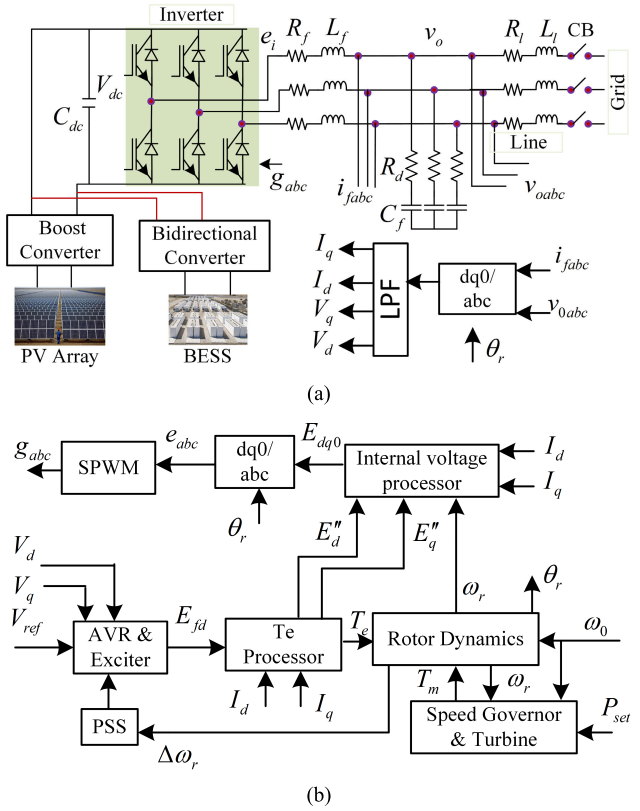


**FIGURE 2.** Proposed controller for the GFMI (a) electric circuit model, (b) GFMI controller.

### B. CONTROLLER PART

Fig. 2(b) shows that the controller of the GFMI consists of two main parts such as (i) frequency controller and (ii) voltage controller. The frequency controller has been developed based on the speed governor and turbine-generator rotor dynamics of an SG. Whereas the voltage controller has been developed based on an AVR and exciter, a PSS, electromagnetic torque ($T_e$) characteristic, and the internal voltage controller of an SG. A provision of the reference voltage ($V_{ref}$) controller can be added using the reactive power ($Q_e$) characteristic of an SG and a PI controller. However, $V_{ref}$ has been directly set in this paper. The development of these controller parts is as follows.

#### 1) FREQUENCY CONTROLLER

Fig. 3 shows the frequency controller of the GFMI. The angular frequency ($\omega_r$) of the GFMI changes if the reference active power ($P_{set}$) and virtual $T_e$ vary. Otherwise, $\omega_r$ remains constant. If $P_{set}$ and $T_e$ vary, the frequency controller tries to maintain the deviation of angular frequency ($\Delta\omega_r$) to zero, i.e., $\Delta\omega_r = 0$. The characteristic of the frequency controller is defined through the negative feedback of angular frequency and two transfer functions $G_{RT}(s)$ and $G_{TG}(s)$ as shown in Fig. 3. $R_p$ in the feedback path in Fig. 3 represents an equivalent speed droop of an SG.

The transfer functions, $G_{RT}(s)$ and $G_{TG}(s)$, depend on the characteristics of the speed governor and turbine-generator

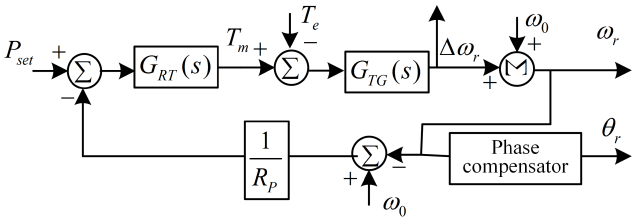


**FIGURE 3.** Proposed frequency controller for the GFMI.

rotor dynamics of an SG, which can be expressed by (17) and (18), respectively.

$$G_{TG}(s) = \frac{s(1+G_2(s))G_1(s)}{s(1+G_2(s)) + K_{12}\omega_0 G_1(s)} \tag{17}$$

$$G_{RT}(s) = \frac{G_{SR}(s)G_{TP}(s)G_2(s)}{1+G_2(s)} \tag{18}$$

where $\omega_0$ is the rated frequency in rad/sec, and $K_{12}$ is the rigidity coefficient between the turbine and generator. The transfer functions $G_1(s)$, $G_2(s)$, $G_{SR}(s)$ and $G_{TP}(s)$ are defined in Appendix. The unit with the transfer function $G_{SR}(s)$ has a bounded output of speed and gain.

#### 2) VOLTAGE CONTROLLER

The voltage controller consists of three parts such as (1) AVR, exciter, and PSS, (2) $T_e$ processor, and (3) internal voltage processor. These three parts are described below.

*(1) AVR, Exciter, and PSS part:* This part of the voltage controller, as shown in Fig. 4, controls the signal $E_{fd}$ which can be expressed as in (19).

$$E_{fd}(s) = G_{AVR}(s)[V_{ref} + G_{PSS}(s)\Delta\omega_r - G_R(s)V_t(s)] \tag{19}$$

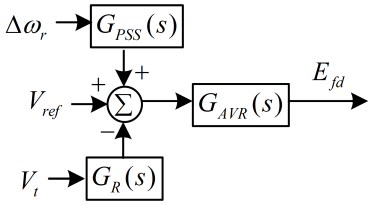


**FIGURE 4.** Exciter, AVR and PSS.

The AVR measures the terminal voltage of the GFMI through a voltage sensor and a voltage signal from a PSS corresponding to the angular frequency deviation ($\Delta\omega_r$) and compares it with $V_{ref}$. The transfer function of the AVR, exciter, PSS, and terminal voltage sensor can be expressed by (20), (21), and (22), respectively.

$$G_{AVR}(s) = \frac{G_A(s)G_E(s)}{1+G_A(s)G_E(s)G_F(s)} \tag{20}$$

$$G_{PSS}(s) = \frac{sK_{STAB}T_w(1+sT_3)(1+sT_1)}{(T_sT_ws^2 + s(T_s+T_w)+1)(1+sT_4)(1+sT_2)} \tag{21}$$

$$G_R(s) = \frac{1}{1+sT_R} \tag{22}$$

where, $G_A(s)$, $G_E(s)$ and $G_F(s)$ are transfer functions of AVR, exciter, and $E_{fd}$ feedback to AVR, which are defined in Appendix. $K_{stab}$ represents the gain of the PSS. $T_s$, $T_w$, $T_1$, and $T_2$ represent time constants in the PSS [30]. $T_R$ represents the time constant of the terminal voltage sensor. The AVR and the PSS have bounded output.

*(2) Electromagnetic torque ($T_e$) processor block:* Fig. 5 shows the $T_e$ processor block which has been designed based on the equivalent sub-transient and transient model of an SG [33]. $T_e$ in Fig. 5 can be expressed as in (23). The two transfer functions $G_{Te\,A}(s)$ and $G_{Te\,B}(s)$ in (24) and (25), respectively, represent the transient and sub-transient characteristics of an SG.

$$T_e(s) = \frac{[G_{Te\,A}(s)E_{fd}s) + G_{Te\,B}(s)I_d(s)]I_q(s)}{\omega_r(s)} \tag{23}$$

$$G_{Te\,A}(s) = G'_d(s)G''_d(s) \tag{24}$$

$$G_{Te\,B}(s) = K_{qd} + K_q G''_q(s) + \frac{G_{TeA}(s)(K_{ds} + K_d G'_d(s))}{G'_d(s)} \tag{25}$$

where the transfer functions $G'_d(s)$, $G''_d(s)$, $G''_q(s)$ and the constants $K_d$, $K_q$, $K_{qp}$, $K_{ds}$, $K_{qd}$, $K_a$ have been defined in Appendix.

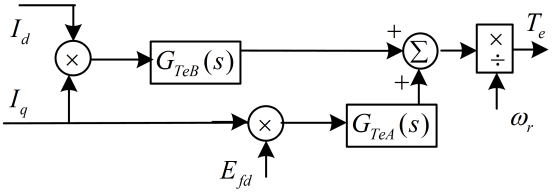


**FIGURE 5.** Electromagnetic torque processor.

*(3) Internal voltage processor block:* The detailed description of this part of the controller has been described in [33] in their previous publication by the authors. The controlled output voltages $E_d$, $E_q$, $E_{dc}$, and $E_{qc}$ in this part of the controller can be expressed as in (26), (27), (28) and (29), respectively, to be used in this paper.

$$E_d(s) = \frac{\omega_r(s)[E''_d(s) + K_{q2p}I_q(s)]}{\omega_0} - K_a I_d(s) \tag{26}$$

$$E_q(s) = \frac{\omega_r(s)[E''_q(s) - K_{d2p}I_d(s)]}{\omega_0} - K_a I_q(s) \tag{27}$$

$$E_{dc}(s) = E''_d(s) + G_{PI}(s)(E_d(s) - V_d(s)) \tag{28}$$

$$E_{qc}(s) = E''_q(s) + G_{PI}(s)(E_q(s) - V_q(s)) \tag{29}$$

Fig. 6 shows the developed controller part based on the mathematical relationships in (26)-(29).

The voltages $E_{dc}$ and $E_{qc}$ obtained from Fig. 6 have been transformed to the *abc*-reference frame using the rotor angle $\theta_r$ obtained from the controller part in Fig. 3. The SPWM module in Fig. 2 converts the *abc* -reference signals to gate pulses for the power electronic switches in the GFMI.

*(4) $V_{ref}$ control:* The desired reactive power generation $Q_{set}$ can be compared with internal reactive power ($Q_e$) measured at the terminal and tuned in a PI block to provide $V_{ref}$. In this paper, $V_{ref}$ has been set directly through $V_{set}$.

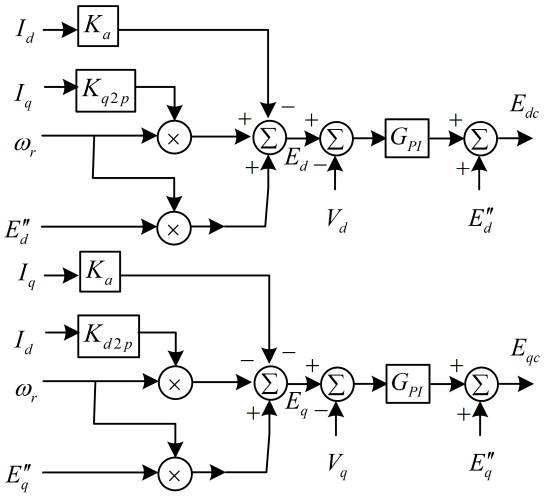


**FIGURE 6.** Internal voltage generator.

### C. DC-LINK VOLTAGE CONTROLLER

From the grid-forming concept, the GFMI is considered as an ideal voltage source, which means the voltage at the dc-link of the GFMI needs to be maintained constant. However, the PV sources are intermittent which causes deviation of the dc-link voltage from its reference value. This might affect the performance of the GFMI. The dc-link voltage deviation can be compensated using the BESS. During any frequency event, the GFMI needs to provide an additional amount of energy that is equivalent to the kinetic energy stored in the rotor of an SG. This additional energy can be provided through the proper control of the BESS as shown in Fig. 7.

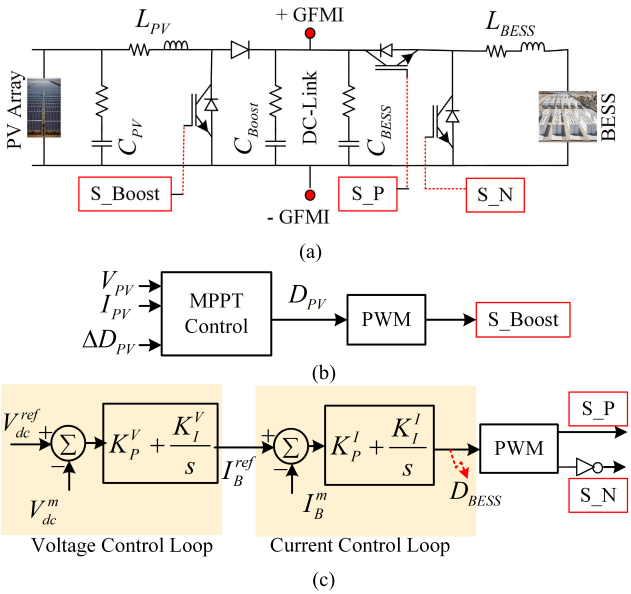


**FIGURE 7.** (a) Circuit diagram of PV- boost and BESS dc-dc converters, (b) dc-dc boost converter controller, (c) BESS controller.

Fig. 7(a) shows the dc-link voltage control circuit, where the PV array and the BESS are connected to the dc-link through a unidirectional boost converter and bidirectional dc-dc converter, respectively. The circuit parameters of the boost and dc-dc converter are provided in Table 1 in the Appendix.

Fig. 7(b) shows the controller for the dc-dc boost converter that boosts up the PV output voltage to the desired voltage level across the dc-link. The dc-dc boost controller uses an MPPT control technique which produces the duty ($D_{PV}$) signal and provides the switching signal S_Boost.

Fig. 7(c) shows the controller for the bidirectional dc-dc converter that compensates for the dc-link voltage deviation through the control of charging and discharging of the BESS. This controller has two loops: (i) voltage control loop and (ii) current control loop. The voltage control loop generates a reference current ($I_B^{ref}$) signal based on the voltage deviation $\Delta V_{dc} = V_{dc}^{ref} - V_{dc}^{m}$, where $V_{dc}^{ref}$ and $V_{dc}^{m}$ are desired reference and measured voltages, respectively, of the dc-link. The current control loop measures the BESS current $I_B^m$ and compares it with $I_B^{ref}$ to produce switching signals S_P and S_N to control the charging/discharging currents of the BESS.

## IV. SIMULATION RESULTS

The circuit model and the controllers of the GFMI of the SG are shown in Fig. 2, and the performance is verified by the simulation of a test system as in Fig. 8, which consists of an SG integrated with the proposed GFMI, an active load of 1.98 MW, and a reactive load of 0.4 MVar, which operates at 6.6 kV and 50 Hz.

Fig. 8 shows that the GFMI generates power at 0.69 kV which is stepped up to 6.6 kV by the Y-Δ step-up transformer.

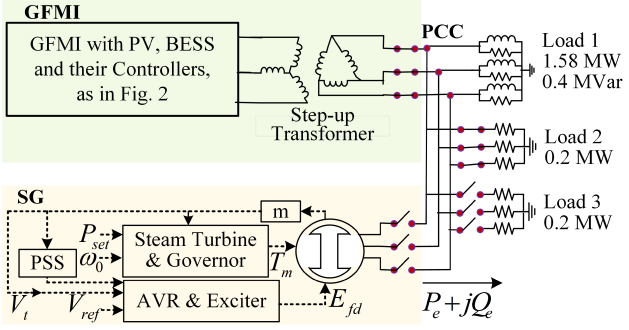


**FIGURE 8.** A test system to evaluate the performance of the proposed controller.

The dc-link reference voltage is $V_{dc}^{ref} = 1.663$ kV which has been slightly adjusted to maintain the PCC voltage and angular frequency of the GFMI system. A modulation index of 0.83 has been considered for the controller of the GFMI to avoid over-modulation during load changes. Since the controller of the GFMI including the LCL filter has been developed as an equivalent system to the SG with its associated control systems, a desired steady-state line-to-line voltage of 6.6 kV at 50 Hz has been ensured by both the GFMI and the SG systems. The GFMI controller has been validated by simulation of the test system in Fig.8 using MATLAB/Simulink environment. The values of the electrical and controller parameters of the test system are available in [33] and in Table 1 in Appendix.

The inertia constants of the GFMI and SG are available in [33], where $H_{GFMI}$ and $H_{SG}$ are different. It is worth noting here that the inverter is an electric switching system whereas the SG is an electromagnetic system. The mathematical model of the SG with its controller parts has been used to design the controller for the GFMI. Therefore, the difference in $H_{GFMI}$ and $H_{SG}$ should be unavoidable. In this paper, the $H_{GFMI}$ of the GFMI is varied to obtain a similar angular frequency of the SG with the $H_{SG}$. The MVA capacities of both systems are kept constant. The relationship between the $H_{GFMI}$ and the $H_{SG}$ follows the expression as in (30).

$$H_{GFMI} = \frac{H_{SG}}{m} \tag{30}$$

where $m$ varies approximately in the range of $0.60 \sim 0.67$. At the lower values of the $H$ constant, $H_{GFMI}$ and $H_{SG}$ exhibit a linear relationship. However, at higher values of the $H$ constant, the relationship between $H_{GFMI}$ and $H_{SG}$ becomes slightly non-linear. The nonlinearity is very slight and can be ignored.

In the simulation, the mechanical input power ($P_{SG}^m$) to SG and the dc input power ($P_{GFMI}^{dc}$) to GFMI have been considered constant (i.e., $\Delta P_{SG}^m = 0$ and $\Delta P_{GFMI}^{dc} = 0$) to test the response performances to frequency events during isolated and parallel operations of the SG and the GFMI. The performances of the SG and GFMI have been elaborately analyzed in Subsections IV-A, IV-B, and IV-C. These analyses prove that the proposed controller for the GFMI emulates the SG perfectly.

The BESS is very important for the grid-forming operation of the GFMI as described in Subsection III-C. The intermittency of solar irradiance (Irr) and dc power compensation from BESS have been simulated and presented in Subsection IV-E, which shows that if the dc-link voltage is maintained constant, the proposed controller for the GFMI can control the voltage and frequency of the formed grid.

### A. STEADY-STATE OPERATION OF THE GFMI AND THE SG

The test system shown in Fig. 8, with load 1 and load 2, has been simulated with the GFMI and the SG separately.

Fig. 9 shows the steady-state current and voltage in pu values in phase-$a$ at the PCC.

The instantaneous current, and voltage wave shapes at the PCC of the GFMI are equal in magnitude and phase to the voltage and current wave shapes at the terminal (PCC) of the SG, respectively. In both cases, the current wave shapes lag by $12.50^0$ from the corresponding voltage wave shapes as seen in Fig. 9. Therefore, it can be concluded that both systems separately maintain a steady-state stable operation while supplying the connected load. A detailed analysis of the steady-state operation of both systems has been described in [33] in their earlier research by the authors.

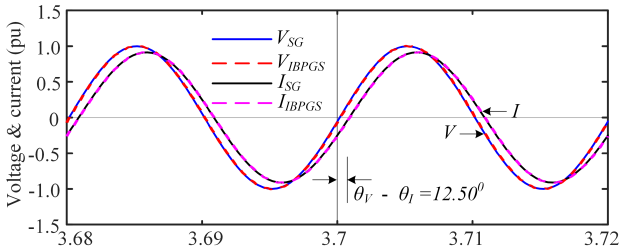


**FIGURE 9.** Comparison of steady-state voltage and current wave shapes of the GFMI and SG.

### B. RESPONSES OF THE GFMI AND THE SG TO LOAD CHANGES

The simulation was running with a total load of 1.8244 MVA and with a lagging power factor of 0.976 while the GFMI and SG were supporting the load separately. The responses of the GFMI and the SG to load changes were observed with the disconnection and addition of an active load of 0.2 MW for a duration of 2 s starting at $t = 4$ s and $t = 10$ s, respectively.

#### 1) FREQUENCY EXCURSION

Fig. 10(a) shows the responses of the angular frequencies of the GFMI and the SG, respectively, due to load changes while they were operating with the inertia constants of $H_{GFMI} = 7.5$ s and $H_{SG} = 5$ s, respectively. A desired steady-state angular frequency of 1 pu has been ensured by both the GFMI and the SG. During the load changes, both the GFMI and the SG respond with the same ROCOF of 0.26 Hz/s, which indicates that both of them possess similar dynamic characteristics. However, their angular frequency excursion slightly differs from each other as shown in Fig. 10(a), which can be decreased by changing the turbine time constants and inertia as described later in this subsection IV-B1. The GFMI and the SG experience an angular frequency excursion of 0.15% with a peak time at 0.605 s and percentage overshoot of 0.025%, and 0.16% with a peak time at 0.696 s and percentage overshoot of 0.07%, respectively, for an 11.24% change in the active load. With the new operating load, both the GFMI and the SG systems attain the new steady-state operating frequencies of 1.0015 pu and 1.0016 pu, respectively, with only a 0.01% steady-state error between the new steady-state operating frequencies.

Fig. 10(b) and (c) show the responses of both GFMI and the SG with varying inertia constants during steady-state and transient periods. The inertia constants of the SG and the GFMI were set at $H_{SG} = [1.5, 3.0, 5.0, 6.75]$ and $H_{GFMI} = [2.5, 5.0, 7.5, 10.0]$ to see their influence on ROCOFs. The ROCOFs measured at those inertia values are 0.534, 0.365, 0.260, and 0.223 Hz/s in transient periods for both systems. The varying inertias also affect the peak time and the percentage overshoot of the angular frequency as shown in Fig. 10(c) which shows that the peak time decreases, and the percentage overshoot increases with decreasing inertia of both the GFMI and the SG. However, the increase in the percentage overshoot of GFMI is lower than that of the SG. The GFMI experiences increasing oscillation in frequency at very low inertia, which might cause the system unstable as described in [33].

The effect of the turbine time constants on the frequency excursion has also been investigated. Three sets of investigation have been performed for three sets of turbine time constants such as $[T_2, T_3, T_4, T_5] = ([0, 0.1, 0.1, 0.1], [0, 0.15, 0.15, 0.15]$ and $[0, 0.1, 1.0, 0.1])$ with $H_{SG} = 1.5$s and $H_{GFMI} = 2.5$s and keeping all other parameters same for both systems as in [33]. With the increasing time constants, the frequency excursions of both systems increase as shown in Fig. 10(d). The peak time and percentage overshoot of both systems increase with increasing time constants as shown in Fig. 10(d). However, the effect of time constants on the frequency excursion is lesser than that of the effect of inertia constants. Also, the time constants do not affect the ROCOF.

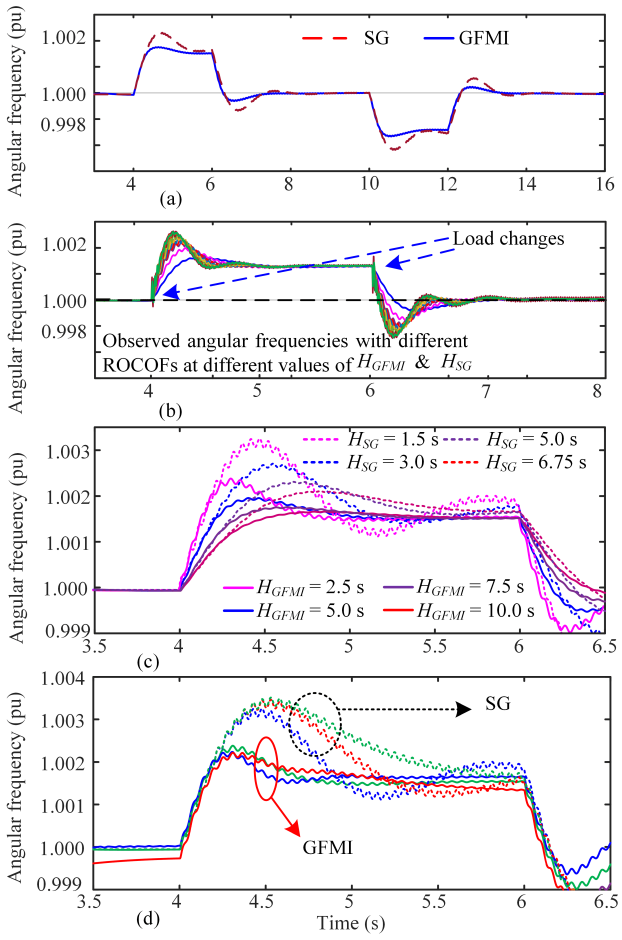


**FIGURE 10.** Comparison of angular frequencies of the GFMI and SG, (a) angular frequency responses at equivalent inertia of the GFMI and the SG to load changes, (b) effect of varying inertias on angular frequencies, (c) zoomed-in angular frequencies in (b), (d) effect of turbine time constants on angular frequencies.

#### 2) TERMINAL VOLTAGE EXCURSION

The terminal voltages of the GFMI and the SG have been observed during the active load changes. The inertia constants

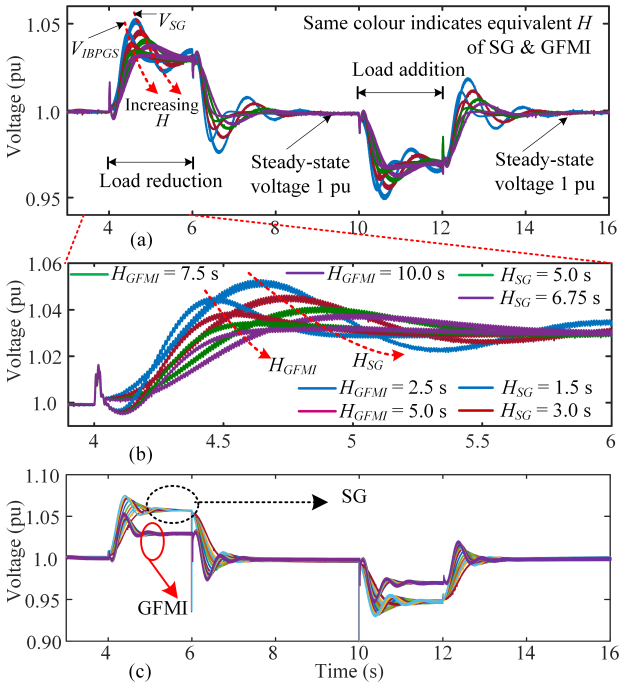


**FIGURE 11.** Comparison of terminal voltages of the GFMI and SG, (a) terminal voltage excursion to load changes, (b) zoomed in of (a), (c) effect of inertia and time constants on terminal voltages during load changes.

of the GFMI and the SG were set at $H_{GFMI} = [2.5, 5, 7.5\ 10]$ and $H_{SG} = [1.5, 3, 5, 6.75]$, respectively, while keeping the turbine constants of both systems the same as 0.1 s. During load changes, both the GFMI and the SG experience a voltage magnitude excursion of approximately 3% for an 11.24% change in active load. With the new load, both the system reaches their new steady-state with a minor steady-state error of 0.56% as shown in Fig. 11(a).

A closer observation of Fig. 11(a) presented in Fig. 11(b) shows that the terminal voltage of the GFMI changes faster than that of the SG. Fig. 11(b) shows that with HGFMI = 2.5s and HSG =1.5s, the terminal voltage of the GFMI reaches the first peak at 0.457 s, whereas the SG takes 0.642 s to reach the first peak. The GFMI has a lower percentage overshoot and settling time than the SG.

The percentage overshoot and the settling time of GFMI were measured as 1.46% and 0.74 s, respectively, whereas the percentage overshoot and the settling time of the SG were measured as 2.24% and 2.36 s. as the turbine constant of the SG is considered low. However, the voltage response times of both the systems to load changes can be reduced by reducing the inertia constants. This has been described in [33] with the setting of inertia constants ranging from 0.2 to 3 s for both the systems, and with the turbine constants of SG to $[T_2, T_3, T_4, T_5] = [0, 10, 3.3, 0.5]$, while keeping the turbine constants of the GFMI as $[T_2, T_3, T_4, T_5] = [0, 0.1, 0.1, 0.1]$. With those new settings, the responses of the terminal voltages of both systems have been observed and presented in Fig. 11(c). Fig. 11(c) shows that although the peak times of the terminal voltage responses reduce with decreasing inertia constants, their percentage overshoots slightly increase. Again, although the terminal voltage excursions of the SG with higher values of turbine constants increase slightly, their settling times decrease.

### 3) POWER OUTPUT

Fig. 12 shows the active and reactive power variations due to the same active load changes as described above. The variation of the inertia constants was the same as $H_{GFMI} = 2.5, 5.0, 7.5, 10$ s and $H_{SG} = 1.5, 3, 5, 6.75$ s while the turbine constants for both systems are kept constants as $[T_2, T_3, T_4, T_5] = [0, 0.1, 0.1, 0.1]$. Figs. 12(a) and (b) show that the peak time and transient overshoot of the active power variations for both the systems are very close which are approximately 0.097 s and 7.14% respectively. The active power transients of both systems are almost similar. However, the peak time, the settling time, and the percentage overshoot of the GFMI are better than that of the SG system, as shown in Fig. 12(c). In steady-state conditions, there is no active power output difference between the two systems.

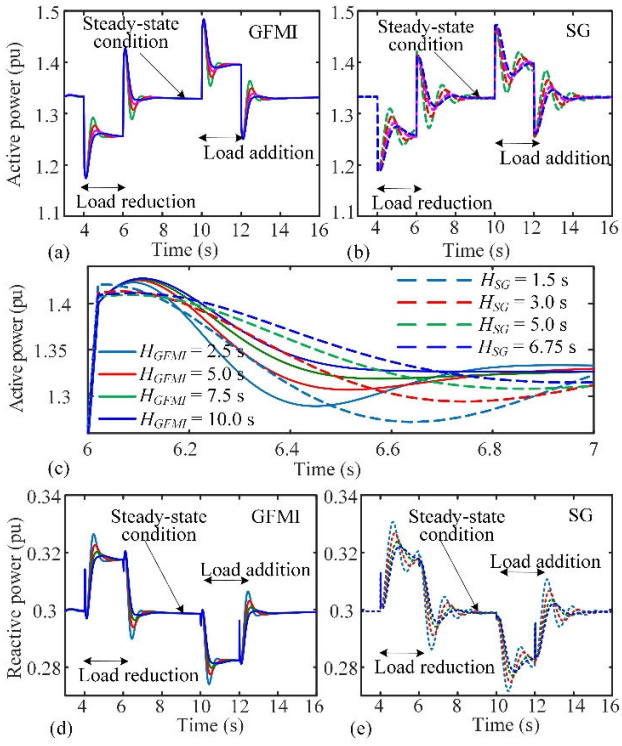


**FIGURE 12.** Power responses to load change (a) active power of GFMI, (b) active power of SG, (c) comparison between responses in (a) and (b), (d) reactive power of GFMI, and (e) reactive power of SG.

Figs. 12(d) and (e) show the reactive power transients during the active load changes for the same parameter settings described above. In the steady-state operating period, both the GFMI and the SG systems are producing the same amount of reactive power. However, the reactive power response of the GFMI is better than the SG.

### C. PARALLEL OPERATION OF THE GFMI WITH THE SG SYSTEMS

In this subsection, the parallel operation of the proposed GFMI with the SG has been investigated during steady-state and transient conditions. Fig. 13 shows the one-line diagram of both the GFMI and the SG systems which can support their loads in isolation. A voltage synchronizer and a connecting switch (SW) have been used for synchronizing the GFMI with the SG system. The parallel operation of the GFMI system with the SG has been investigated under two scenarios such as (i) parallel operation while the MVA capacities of both the GFMI and the SG are equal, and (ii) parallel operation while the MVA capacities of the GFMI and the SG are unequal. For both scenarios, the transient responses of the GFMI and the SG after synchronization have also been observed.

#### 1) SYNCHRONIZATION OF THE GFMI WITH THE SG SYSTEMS

A voltage synchronizer, as shown in Fig. 13, is used to observe the magnitudes and phases of the terminal voltages of the GFMI and the SG systems.

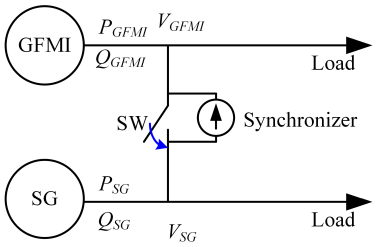


**FIGURE 13.** A GFMI system is connecting in parallel with the SG system.

Fig. 14(b) shows the observed voltage waveshapes at the terminal of the GFMI and the SG. The terminal voltage ($V_{GFMI}$) of the GFMI reaches the same magnitude as that of the SG's terminal voltage ($V_{SG}$) after 2.0 s of starting the GFMI system. However, the GFMI controller takes another few fractions of seconds to bring the $V_{GFMI}$ in phase with the $V_{SG}$. Fig. 14(a) shows that although the magnitudes of terminal voltages of both the GFMI and the SG are equal, they have phase differences. The voltages appear in phase, 2.7s after starting the GFMI and maintaining synchronism with the SG system as shown in Fig. 14(c).

#### 2) TRANSIENT RESPONSES OF THE GFMI AND THE SG IN PARALLEL OPERATION

When the $V_{GFMI}$ and $V_{SG}$ become equal in magnitude and are in phase, the synchronizing switch (SW) can be turned on to connect the GFMI system in parallel with the SG system. In this part of the simulation, the synchronizing switch is turned on at 3.8 s, and four frequency events have been introduced at 6.5, 9.0, 11.5, and 14.0 s through load changes. Fig. 15 shows the transients in angular frequencies, active and reactive power outputs after synchronization, and load variations while the GFMI and the SG are running in parallel.

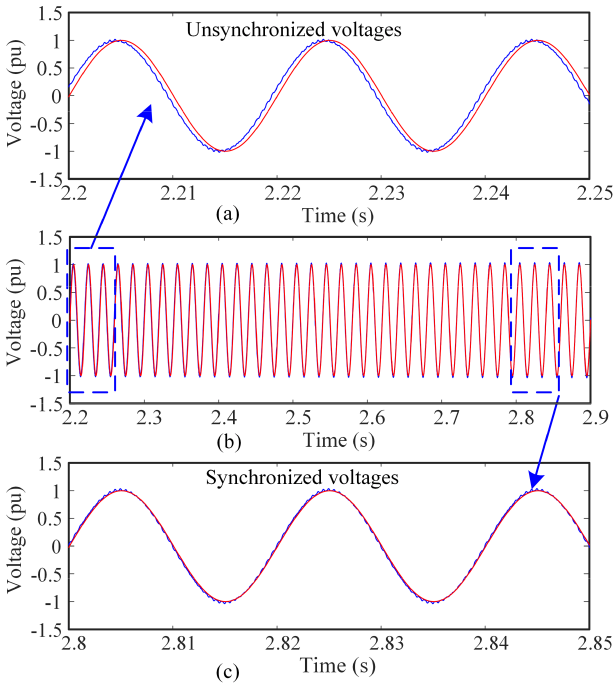


**FIGURE 14.** Voltage wave shapes in phase-a before and after synchronization of the GFMI and SG.

Two load scenarios have been considered in the simulation. In load scenario 1, the GFMI and the SG equally support a total active power load of 3.56 MW and reactive power load of 0.8 MVAr, and a 0.4 MW load variation is considered. In load scenario 2, the GFMI supports 20.21% of a total active power load of 8.8056 MW while keeping the same 0.8 MVAr reactive power load and 0.4 MW load variation as in load scenario 1. An angular base frequency of $100\pi$ rad/s, an MVA base of 2 MVA, and a voltage base of 6.6 kV have been considered for all the measurements.

Fig. 15(a) and Fig. 15(b) show the transients in angular frequencies of the GFMI and the SG while each of them is sharing equally (scenario 1) and unequally (scenario 2) of the total load, respectively. The transients appear in angular frequencies of both the GFMI and the SG after the synchronization switch is turned on at 3.8 s after starting the simulation. Fig. 15(a) shows that both the GFMI and the SG oscillate in opposite directions with a very negligible frequency excursion in the first peaks of oscillations. However, when the GFMI is smaller than the SG, the frequency excursion of the GFMI after synchronization is larger than that of the SG, as shown in Fig. 15(b). The oscillations after synchronization diminish quickly and the angular frequencies in both the load scenario reach a steady-state value of 1 pu. The oscillations in active and reactive power outputs in both the load scenario of the GFMI and the SG after synchronization are almost similar as shown in Fig. 15(c) and Fig. 15(d).

According to the amount of load variation, the active power load variations are 11.24% and 4.54% of the total active load in load scenarios 1 and 2, respectively. Therefore, the

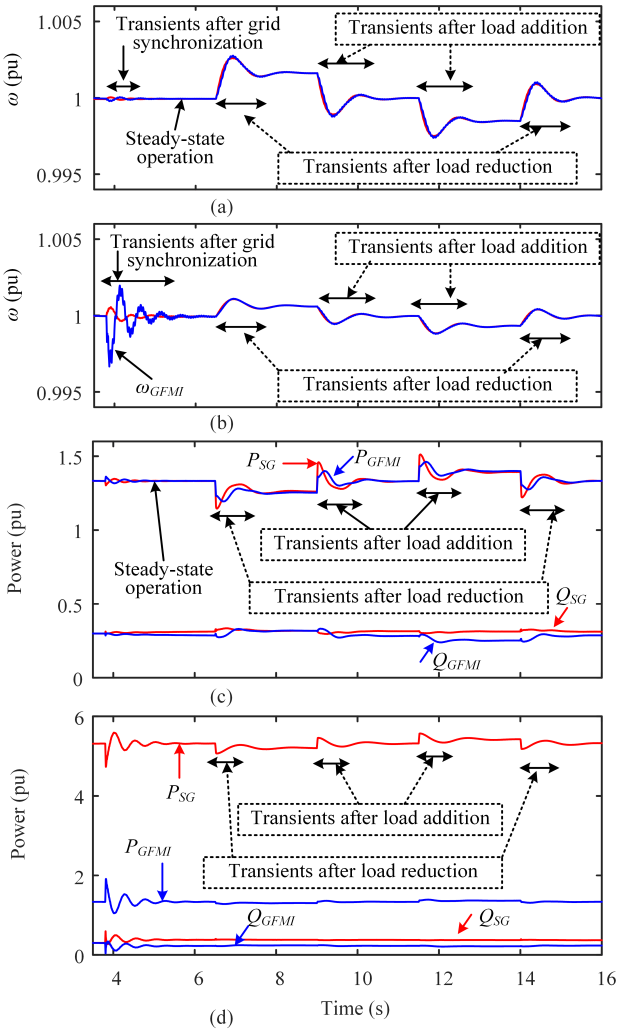


**FIGURE 15.** Transients responses of the GFMI and SG during synchronization and load changes while in parallel operation (a) angular frequency in load scenario 1, (b) angular frequency transients in load scenario 2, (c) active and reactive load sharing in load scenario 1, and (d) active an reactive load sharing in load scenario 2.

frequency excursion in Fig. 15(a) is larger than that in Fig. 15(b). The percent overshoots in angular frequency transients are 0.0998% and 0.04998% in load scenarios 1 and 2, respectively. However, the frequencies change similarly in both load scenarios and reach a new steady-state value after each frequency event. During load reduction, the angular frequencies of both the GFMI and SG increase by 0.16% in load scenario 1 and 0.053% in load scenario 2. On the other hand, during load addition, the angular frequencies of both the GFMI and the SG decreased by 0.16% in load scenario 1 and 0.053% in load scenario 2.

Fig. 15(c) and Fig. 15(d) show the transients in load sharing by the GFMI and the SG in load scenarios 1 and 2, respectively. In load scenario 1, both the GFMI and the SG are sharing the load variations equally as they are similar in MVA capacities. However, as the MVA capacity of the SG is larger than the GFMI in load scenario 2, the SG is supporting a larger load than the GFMI. In both load scenarios, the SG has a larger percent overshoot during each frequency event. There was no reactive power load variation, and there are very minor transients in reactive power, as shown in Fig. 15(c) and Fig. 15(d).

#### 3) TRANSIENT RESPONSE TO A THREE-PHASE FAULT

During parallel operation of the GFMI and the SG, a three-phase to ground fault was initiated at t = 8 s for a duration of 150 ms at the terminal of the SG. Fig. 16 shows the transient responses of the GFMI and the SG. Fig. 16(a) shows that both the GFMI and SG have the same transient response in response to the fault at their terminal.

The terminal voltages of both the GFMI and the SG reduce to zero during the fault, and they regain a steady value after fault removal. Figs. 16(b) and (c) show the currents from the GFMI and the SG, respectively, during normal and fault conditions. During normal parallel operation, the currents from both the GFMI and SG are the same as they are sharing the same load. The fault currents also follow the same transient patterns. However, the SG provides a higher fault current than the GFMI. One of the biggest challenges of GFMI is to withstand high fault currents. To limit the high fault current from the GFMI, a fault limiter [37], [38], [39], [40], [41] can be used to protect the power electronic switches in the GFMI.

Figs 16(d) and (e) show the active and reactive power supply from the GFMI and SG, respectively. During normal and fault periods, both the GFMI and SG show the same characteristics of active and reactive power. However, the active and reactive power transients become slightly different after fault removal. Fig. 16(f) shows the transients in angular frequencies of the GFMI and SG, which have a similar pattern. The angular frequency of the GFMI has a larger amplitude of oscillation than that of the SG. However, the oscillations in angular frequencies diminish with time and reach steady-state values.

### D. ISLANDING OPERATION OF THE GFMI FROM THE SG SYSTEM

To check the performance of the proposed GFMI in islanded mode, the same system as shown in Fig. 13 has been considered. Fig. 17 shows the voltage waveforms at the PCC during three operating modes of the GFMI in different time scales. Fig. 17(a) shows the voltage at the PCC of the GFMI at the black start or pre-synchronization mode, which shows the GFMI is improving its terminal voltage in magnitude and phase to exactly match with the grid voltage for synchronization. Fig. 17(b) shows that the terminal voltage of the GFMI exactly matches with the system voltage, and hence the GFMI is connected to the grid at t = 3.8 s by switching on the switch (SW) as shown in Fig. 13. At grid-connected mode, the system was running at stead-state.

For islanded mode of operation of the GFMI, the switch (SW) in Fig. 13 was tripped at t = 8 s. Fig. 17(c) shows the voltage at the PCC before and after switching the switch (SW) at t = 8 s. After the transition from grid-connected to

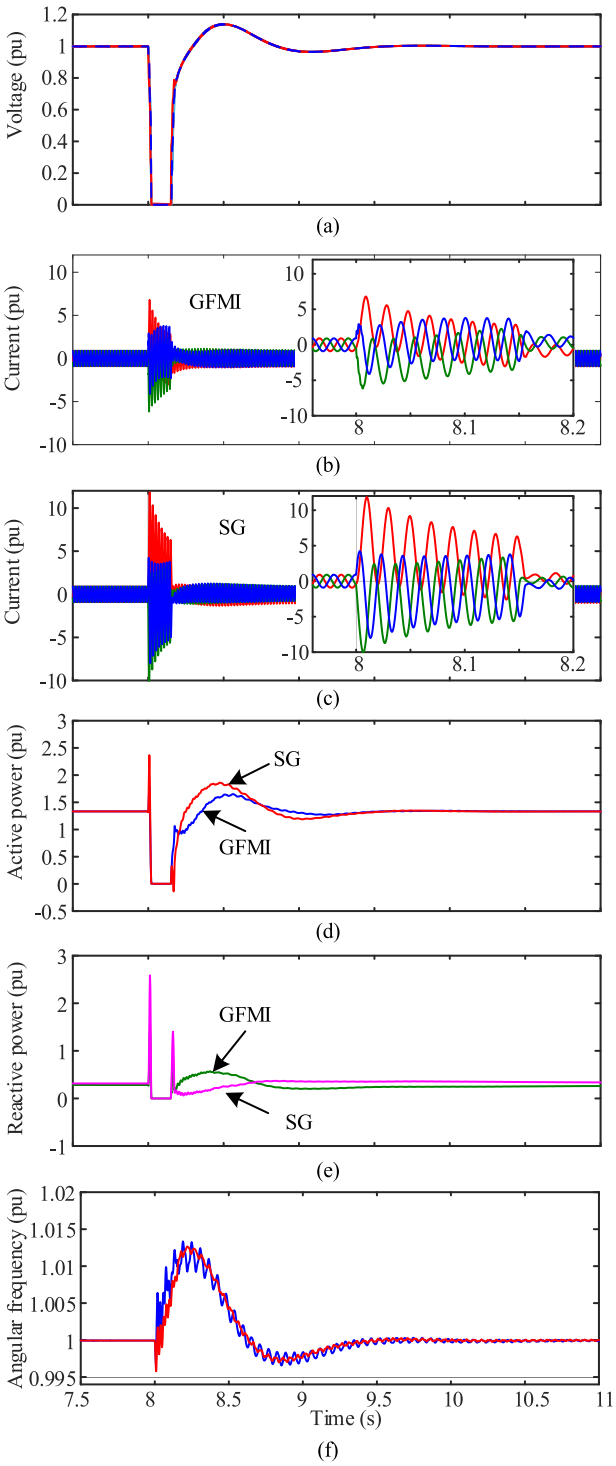


**FIGURE 16.** Transient responses of GFMI and SG to three-phase to ground fault (a) terminal voltages, (b) fault current contribution of the GFMI to fault, (c) fault current contribution of the SG to the fault, (d) active powers, (e) reactive powers, and (f) angular frequencies.

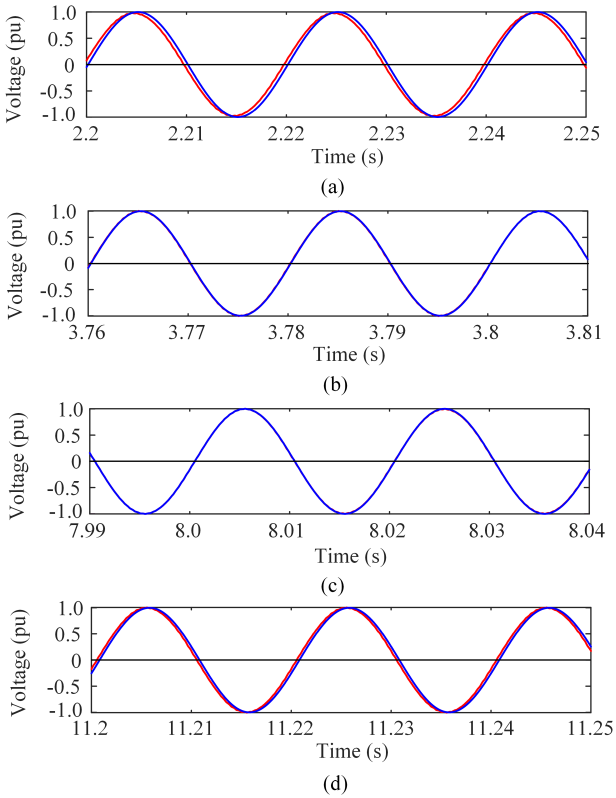


**FIGURE 17.** PCC voltage of the GFMI, (a) voltage before grid-connection, (b) voltage before and after grid-connection, (c) voltage before and after islanding, and (d) voltage during islanded mode of operation.

islanded mode operation of the GFMI its terminal voltage at the PCC starts changing to a new operating voltage at the islanded mode with its own load. However, as the total load of the GFMI is not varied, there is minor change in phase of the PCC voltage of the GFMI compared to the system voltage as shown in Fig. 17(d). Fig. 17 shows that during grid-connection and grid-isolation of the GFMI, the PCC voltage does not experience any transient which may affect the operation of the GFMI during grid-connected or grid-isolated mode.

Fig. 18 shows the transients in the angular frequencies ($\omega_{GFMI}$ and $\omega_{SG}$) and active ($P_{GFMI}$ and $P_{SG}$) and reactive ($Q_{GFMI}$ and $Q_{SG}$) power output from the GFMI and the SG, respectively.

The transients in angular frequencies and output powers have already been discussed in Fig. 15. However, Fig. 18 shows together the three operating modes such as before grid-connection, during grid-connection and after grid-isolation to compare the performances of the GFMI with the SG. Fig. 18 shows that both the GFMI and the SG were running in steady-state maintaining the load-generation balance. When the grid-isolation mode is activated through the switch (SW), there occurs a power mismatch which causes a transient in the angular frequencies of both the GFMI and the SG as shown in Fig. 18(a). The transients in the active and reactive powers at grid-isolation are minor as shown in Fig. 18(c). To clearly visualize the transients at grid-isolation, both the active and reactive power outputs from the GFMI and the SG have been zoomed in as shown in Fig. 18(b) and Fig. 18(d), respectively. Although the transients appear during grid-isolation of the

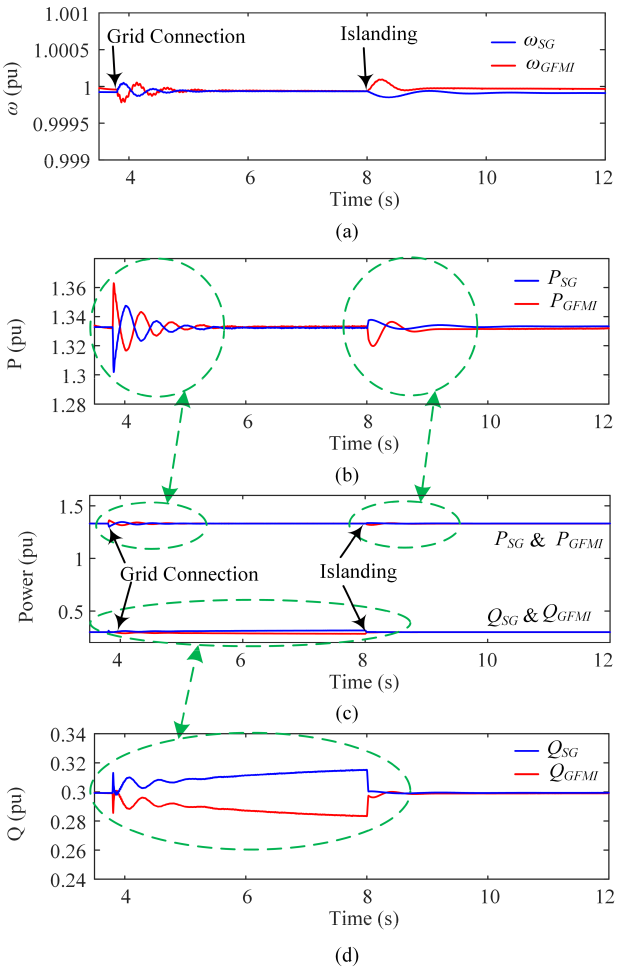


**FIGURE 18.** Transient responses of the GFMI and the SG during grid-connection and grid-isolation, (a) transients in angular frequencies, (b) transients in active power outputs, (c) transients in active and reactive power outputs together, and (d) transients in reactive power outputs.

GFMI, they disappear shortly, and both the GFMI and SG reach their steady-state operation as shown in Fig. 18.

### E. PERFORMANCE OF THE GFMI IN RESPONSE TO PV INTERMITTENCY

Fig. 19 shows the performance measurement at the dc-link side of the GFMI. The irradiance profile as shown in Fig. 19(a) has been simulated to demonstrate the PV power intermittent and how the BESS compensates for the power deviation to maintain the dc-link voltage constant.

Fig. 19(b) shows that when Irr is high (before 12 s and after 25 s of simulation time), the PV system is producing enough power to support the load and to charge the BESS. In these periods, the battery power ($P_{Battery}$) is negative which indicates the battery is in charging mode, and the battery charging mode is indicated by the increasing state of charge (SOC) of the battery in Fig. 19(d) and the battery negative current ($-I_B^m$ and $-I_B^{ref}$) in Fig. 19(e). From 12 s to 25 s of the simulation time, the Irr is low, and the battery is in discharge mode to compensate for power deviation to support the load. During discharge mode, the $P_{Battery}$ is positive, as shown in Fig. 19(b), which is indicated by decreasing SOC in Fig. 19(d) and battery positive current ($+I_B^m$ and $+I_B^{ref}$) in Fig. 19(e). Charging and discharging the BESS helps maintain the dc-link voltage constant. Fig. 19(c) shows that at every instant the Irr changes, the $V_{dc}^m$ deviates from $V_{dc}^{ref}$. However, the BESS helped bring $V_{dc}^m$ back to $V_{dc}^{ref}$.

Fig. 20 shows the performance measurement at the ac side of the GFMI. Fig. 20(a) shows the active ($P_{PCC}$) and reactive ($Q_{PCC}$) power output from the GFMI. In every instance of Irr change, there is a deviation in $P_{PCC}$ and $Q_{PCC}$, which is equivalent to the deviation in $P_{PV}$. The impact of $\Delta P_{PV}$ is also observed in PCC voltage ($V_{PCC}$) in Fig. 20(b) and frequency in Figs. 20(c) and 20(d). However, the BESS compensate the $\Delta P_{PV}$ and help bring $P_{PCC}$, $Q_{PCC}$, $V_{PCC}$, $\omega_r$, and $F_r$ back to their steady-state value, as shown in Fig. 20.

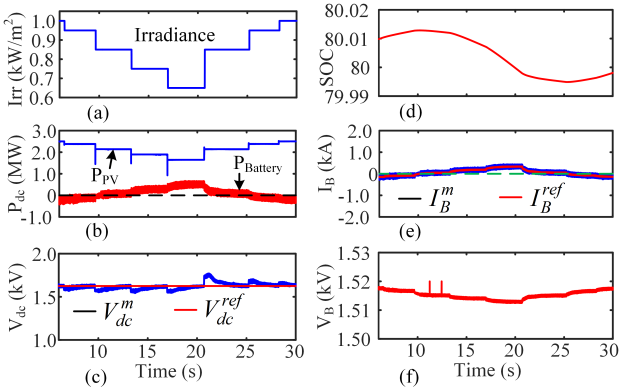


**FIGURE 19.** Performance parameters at the dc-link side of the GFMI (a) Irr, (b) $P_{PV}$ and $P_{Battery}$, (c) dc-link voltage, (d) SOC, (e) charging and discharging current of BESS, (f), BESS voltage.

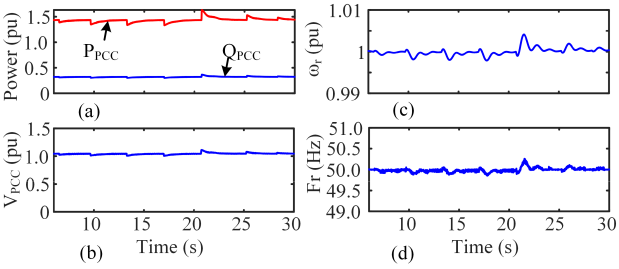


**FIGURE 20.** Performance parameters at the ac side of the GFMI (a) $P_{PCC}$ and $Q_{PCC}$, (b) $V_{PCC}$, (c) $\omega_r$, (d) $F_r$.

## V. CONCLUSION

This paper proposes a grid-forming controller for IBPGSs that can enable IBPGSs to mimic SGs when connected to a grid, to maintain the voltage and frequency of the power systems. A mathematical relationship of inertia support from the grid-forming IBPGS has been developed to have similar characteristics of an SG to support the increasing penetration of

grid-following IBPGSs to grid. The proposed controller has been validated by simulation in isolated and grid-connected operations. The responses of the grid-forming IBPGS during steady-state and transient conditions in the grid, and during PV intermittency have been compared with that of an actual SG. The comparison confirms the ability of the grid-forming IBPGS to form grid similar to an SG does to maintain grid dynamics for the stable operation of the grid-following IBPGSs during transient conditions due to load change and faults. The results show that using the proposed grid-forming controller, the PLL can operate correctly during slow and fast frequency variations instigated by the frequency events in isolated and grid-connected operations. As the proposed grid-forming IBPGS can provide virtual inertia like an SG when a BESS is used, it is anticipated that the proposed grid-forming controller will be able to form an isolated grid, operate in parallel with other grid-forming SGs, and help in inertia support to the power system to ensure the stable operation of the power grid integrated with grid-following IBPGSs which share a large load in the systems.

## APPENDIX

In this paper, an SG has been emulated through a GFMI. The controller part of the GFMI is based on the mathematical model of a steam turbine generator and its controller parts such as AVR, exciter, and PSS. In the modeling, a four-mass turbine section with its accessories has been considered. The parameters which are used in the simulations to prove the performance of the proposed GFMI controller are available in [33] by the authors. All the fundamental parameters are defined according to the definitions given in [30].

**TABLE 1. Circuit and control parameters of the PV-boost and BESS DC-DC converter.**

| | | | | | |
|---|---|---|---|---|---|
| $C_{PV}$ | 100 µF | $C_{BESS}$ | 4700 µF | $K_I^V$ | 1.5 |
| $L_{PV}$ | 5 mH | $L_{BESS}$ | 0.5 mH | $K_P^I$ | 0.01 |
| $C_{Boost}$ | 4700 µF | $K_P^V$ | 0.85 | $K_I^I$ | 10 |

Speed governor turbine-generator rotor dynamic:

$$G_{TG}(s) = \frac{s(1+G_2(s))G_1(s)}{s(1+G_2(s)) + K_{12}\omega_0 G_1(s)},$$
$$G_1(s) = \frac{1}{2H_1 s + K_D}$$
$$G_{RT}(s) = \frac{G_{SR}(s)G_{TP}(s)G_2(s)}{1+G_2(s)},$$
$$G_{SR}(s) = \frac{K_P}{(1+sT_{SR})(1+sT_{SM})}$$
$$G_{TP}(s) = (G_{T5}(s)G_5(s)G_4(s) + G_{T4}(s)G_4(s) + G_{T3}(s))G_3(s) + G_{T2}(s),$$
$$G_{T5}(s) = G_{CH}(s)F_5, G_{T4}(s) = G_{CH}(s)G_{RH1}(s)F_4$$
$$G_{T3}(s) = G_{CH}(s)G_{RH1}(s)G_{RH2}(s)F_3$$
$$G_{T2}(s) = G_{CH}(s)G_{RH1}(s)G_{RH2}(s)G_{RH3}(s)F_2$$
$$G_2(s) = G_{2i}(s)K_{12}, G_{2i}(s) = \frac{G_{H2}(s)}{1+K_{23}(1-G_3(s))G_{H2}(s)},$$
$$G_3(s) = G_{3i}(s)K_{23}, G_{3i}(s) = \frac{G_{31}(s)}{1+K_{34}(1-G_4(s))G_{31}(s)}$$
$$G_4(s) = G_{4i}(s)K_{34}, G_{4i}(s) = \frac{G_{41}(s)}{1+K_{45}(1-G_5(s))G_{41}(s)}$$
$$G_5(s) = G_{51}(s)K_{45}, G_{51}(s) = \frac{G_{H5}(s)}{1+K_{45}G_{H5}(s)}$$
$$G_{41}(s) = \frac{G_{H4}(s)}{1+K_{34}G_{H4}(s)}, \quad G_{31}(s) = \frac{G_{H3}(s)}{1+K_{23}G_{H3}(s)}$$
$$G_{H3}(s) = \frac{\omega_0}{s(2H_3 s + D_3)}, \quad G_{H2}(s) = \frac{\omega_0}{s(2H_2 s + D_2)}$$
$$G_{H5}(s) = \frac{\omega_0}{s(2H_5 s + D_5)}, \quad G_{H4}(s) = \frac{\omega_0}{s(2H_4 s + D_4)}$$
$$G_{CH}(s) = \frac{1}{1+sT_{CH}}, \quad G_{RH1}(s) = \frac{1}{1+sT_{RH1}},$$
$$G_{RH2}(s) = \frac{1}{1+sT_{RH2}}$$
$$G_{RH3}(s) = \frac{1}{1+sT_{RH3}}$$

AVR, exciter, and PSS:

$$G_A(s) = \frac{K_A}{1+sT_A} \quad G_E(s) = \frac{1}{K_E + sT_E} \quad G_F(s) = \frac{sK_F}{1+sT_F}$$

$T_e$ Processor:

$$K_d = x_d - x'_d, \quad K_q = x_q - x''_q,$$
$$K_{qp} = x'_q, \quad K_{ds} = x'_d - x''_d$$
$$K_{qd} = x''_q - x''_d, K_a = R_a$$
$$G'_d(s) = \frac{1}{1+sT'_{d0}}, \quad G''_d(s) = \frac{1}{1+sT''_{d0}}, \; G''_q(s) = \frac{1}{1+sT''_{q0}}$$

## REFERENCES

[1] J. Matevosyan, B. Badrzadeh, T. Prevost, E. Quitmann, D. Ramasubramanian, H. Urdal, S. Achilles, J. MacDowell, S. H. Huang, V. Vital, J. O'Sullivan, and R. Quint, "Grid-forming inverters: Are they the key for high renewable penetration?" *IEEE Power Energy Mag.*, vol. 17, no. 6, pp. 89–98, Nov. 2019.

[2] A. Blakers, B. Lu, and M. Stocks, "100% renewable electricity in Australia," Austral. Nat. Univ., Canberra, ACT, Australia, Tech. Rep., Feb. 2017. [Online]. Available: http://energy.anu.edu.au/files/100%25%20renewable%20electricity%20in%20Australia.pdf

[3] Y. P. Agalgaonkar, B. C. Pal, and R. A. Jabr, "Distribution voltage control considering the impact of PV generation on tap changers and autonomous regulators," *IEEE Trans. Power Syst.*, vol. 29, no. 1, pp. 182–192, Jan. 2014.

[4] F. Milano, F. Dörfler, G. Hug, D. J. Hill, and G. Verbič, "Foundations and challenges of low-inertia systems," in *Proc. Power Syst. Comput. Conf. (PSCC)*, Jun. 2018, pp. 1–25.

[5] R. Teodorescu, M. Liserre, and P. Rodriguez, *Grid Converters for Photovoltaic and Wind Power Systems*. Hoboken, NJ, USA: Wiley, 2011.

[6] X. Wang, L. Harnefors, and F. Blaabjerg, "Unified impedance model of grid-connected voltage-source converters," *IEEE Trans. Power Electron.*, vol. 33, no. 2, pp. 1775–1787, Feb. 2018.

[7] Y. Sun, E. de Jong, X. Wang, D. Yang, F. Blaabjerg, V. Cuk, and J. Cobben, "The impact of PLL dynamics on the low inertia power grid: A case study of Bonaire island power system," *Energies*, vol. 12, no. 7, p. 1259, Apr. 2019.

[8] M. Nedd, J. Browell, K. Bell, and C. Booth, "Containing a credible loss to within frequency stability limits in a low-inertia GB power system," *IEEE Trans. Ind. Appl.*, vol. 56, no. 2, pp. 1031–1039, Mar. 2020.

[9] H. T. Nguyen, G. Yang, A. H. Nielsen, and P. H. Jensen, "Combination of synchronous condenser and synthetic inertia for frequency stability enhancement in low-inertia systems," *IEEE Trans. Sustain. Energy*, vol. 10, no. 3, pp. 997–1005, Jul. 2019.

[10] X. Zhao, L. Chang, R. Shao, and K. Spence, "Power system support functions provided by smart inverters—A review," *CPSS Trans. Power Electron. Appl.*, vol. 3, no. 1, pp. 25–35, Mar. 2018.

[11] X. Wang, J. Yao, J. Pei, P. Sun, H. Zhang, and R. Liu, "Analysis and damping control of small-signal oscillations for VSC connected to weak AC grid during LVRT," *IEEE Trans. Energy Convers.*, vol. 34, no. 3, pp. 1667–1676, Sep. 2019.

[12] W. Du, R. H. Lasseter, and A. S. Khalsa, "Survivability of autonomous microgrid during overload events," *IEEE Trans. Smart Grid*, vol. 10, no. 4, pp. 3515–3524, Jul. 2019.

[13] Q. Zhong, "Power-electronics-enabled autonomous power systems: Architecture and technical routes," *IEEE Trans. Ind. Electron.*, vol. 64, no. 7, pp. 5907–5918, Jul. 2017.

[14] U. Tamrakar, D. Shrestha, M. Maharjan, B. Bhattarai, T. Hansen, and R. Tonkoski, "Virtual inertia: Current trends and future directions," *Appl. Sci.*, vol. 7, no. 7, p. 654, Jun. 2017.

[15] P. J. Hart, J. Goldman, R. H. Lasseter, and T. M. Jahns, "Impact of harmonics and unbalance on the dynamics of grid-forming, frequency-droop-controlled inverters," *IEEE J. Emerg. Sel. Topics Power Electron.*, vol. 8, no. 2, pp. 976–990, Jun. 2020.

[16] S. S. Guggilam, C. Zhao, E. Dall'Anese, Y. C. Chen, and S. V. Dhople, "Optimizing power–frequency droop characteristics of distributed energy resources," *IEEE Trans. Power Syst.*, vol. 33, no. 3, pp. 3076–3086, May 2018.

[17] B. John, A. Ghosh, and F. Zare, "Load sharing in medium voltage islanded microgrids with advanced angle droop control," *IEEE Trans. Smart Grid*, vol. 9, no. 6, pp. 6461–6469, Nov. 2018.

[18] H. Moussa, A. Shahin, J. Martin, S. Pierfederici, and N. Moubayed, "Optimal angle droop for power sharing enhancement with stability improvement in islanded microgrids," *IEEE Trans. Smart Grid*, vol. 9, no. 5, pp. 5014–5026, Sep. 2018.

[19] M. Ashabani and J. Jung, "Synchronous voltage controllers: Voltage-based emulation of synchronous machines for the integration of renewable energy sources," *IEEE Access*, vol. 8, pp. 49497–49508, 2020.

[20] M. Ebrahimi, S. A. Khajehoddin, and M. Karimi-Ghartemani, "An improved damping method for virtual synchronous machines," *IEEE Trans. Sustain. Energy*, vol. 10, no. 3, pp. 1491–1500, Jul. 2019.

[21] J. Roldán-Pérez, A. Rodríguez-Cabero, and M. Prodanovic, "Design and analysis of virtual synchronous machines in inductive and resistive weak grids," *IEEE Trans. Energy Convers.*, vol. 34, no. 4, pp. 1818–1828, Dec. 2019.

[22] M. Li, W. Huang, N. Tai, L. Yang, D. Duan, and Z. Ma, "A dual-adaptivity inertia control strategy for virtual synchronous generator," *IEEE Trans. Power Syst.*, vol. 35, no. 1, pp. 594–604, Jan. 2020.

[23] M. Colombino, D. Groß, J. Brouillon, and F. Dörfler, "Global phase and magnitude synchronization of coupled oscillators with application to the control of grid-forming power inverters," *IEEE Trans. Autom. Control*, vol. 64, no. 11, pp. 4496–4511, Nov. 2019.

[24] P. Li, J. Ji, H. Ji, J. Jian, F. Ding, J. Wu, and C. Wang, "MPC-based local voltage control strategy of DGs in active distribution networks," *IEEE Trans. Sustain. Energy*, vol. 11, no. 4, pp. 2911–2921, Oct. 2020.

[25] Q.-C. Zhong and G. Weiss, "Synchronverters: Inverters that mimic synchronous generators," *IEEE Trans. Ind. Electron.*, vol. 58, no. 4, pp. 1259–1267, Apr. 2011.

[26] R. H. Lasseter, Z. Chen, and D. Pattabiraman, "Grid-forming inverters: A critical asset for the power grid," *IEEE J. Emerg. Sel. Topics Power Electron.*, vol. 8, no. 2, pp. 925–935, Jun. 2020.

[27] L. Harnefors, X. Wang, A. G. Yepes, and F. Blaabjerg, "Passivity-based stability assessment of grid-connected VSCs—An overview," *IEEE J. Emerg. Sel. Topics Power Electron.*, vol. 4, no. 1, pp. 116–125, Mar. 2016.

[28] *IEEE Guide for Planning DC Links Terminating at AC Locations Having Low Short-Circuit Capacities*, IEEE Standard 1204-1997, 1997.

[29] P. Zhou, X. Yuan, J. Hu, and Y. Huang, "Stability of DC-link voltage as affected by phase locked loop in VSC when attached to weak grid," in *Proc. IEEE PES Gen. Meeting | Conf. Expo.*, Jul. 2014, pp. 1–5.

[30] P. Kundur, *Power System Stability and Control*, vol. 4, no. 2, N. J. Balu and M. G. Lauby, Eds. New York, NY, USA: McGraw-Hill, 1994.

[31] M. H. Rashid, *Power Electronics Handbook*. Oxford, U.K.: Butterworth-Heinemann, 2010.

[32] *IEEE Recommended Practice and Requirements for Harmonic Control in Electric Power Systems*, IEEE Standard 519-2014 (Revision of IEEE Std 519-1992), Jun. 2014, pp. 1–29.

[33] M. M. Islam, K. M. Muttaqi, D. Sutanto, M. M. Rahman, and O. Alonso, "Controller design for grid forming inverter-based power generating systems to behave as synchronous machines," in *Proc. IEEE Ind. Appl. Soc. Annu. Meeting (IAS)*, Oct. 2021, pp. 1–7.

[34] L. R. Castillo and A. Roscoe, "Experimental validation of a novel inertia-less VSM algorithm," in *Proc. IEEE Power Energy Soc. Innov. Smart Grid Technol. Conf. (ISGT)*, Feb. 2018, pp. 1–5.

[35] M. Yu, A. J. Roscoe, C. D. Booth, A. Dysko, R. Ierna, J. Zhu, N. Grid, and H. Urdal, "Use of an inertia-less virtual synchronous machine within future power networks with high penetrations of converters," in *Proc. Power Syst. Comput. Conf. (PSCC)*, Jun. 2016, pp. 1–7.

[36] Y. Chen, R. Hesse, D. Turschner, and H. Beck, "Improving the grid power quality using virtual synchronous machines," in *Proc. Int. Conf. Power Eng., Energy Electr. Drives*, May 2011, pp. 1–6.

[37] M. M. Islam, K. M. Muttaqi, and D. Sutanto, "Parameter design and performance analysis of a saturated amorphous alloy core based fault current limiter for power grid applications," in *Proc. IEEE Ind. Appl. Soc. Annu. Meeting (IAS)*, Oct. 2021, pp. 1–6.

[38] M. M. Islam, K. M. Muttaqi, and D. Sutanto, "A saturated amorphous alloy core-based inrush current limiter to eliminate inrush currents and restrain harmonics during transformer energization," *IEEE Trans. Ind. Appl.*, vol. 57, no. 6, pp. 6634–6645, Nov. 2021.

[39] M. M. Islam, K. M. Muttaqi, and D. Sutanto, "A novel saturated amorphous alloy core based fault current limiter for improving the low voltage ride through capability of doubly-fed induction generator based wind turbines," *IEEE Trans. Ind. Appl.*, vol. 57, no. 3, pp. 2023–2034, May 2021.

[40] M. M. Islam, K. M. Muttaqi, and D. Sutanto, "A saturated amorphous alloy core based smart fault current limiter for improving the low voltage ride through capability of distributed generation units," in *Proc. IEEE Ind. Appl. Soc. Annu. Meeting*, Detroit, MI, USA, Oct. 2020, pp. 1–6.

[41] M. M. Islam, K. M. Muttaqi, and D. Sutanto, "A saturated amorphous alloy core-based inrush current limiter," in *Proc. IEEE Ind. Appl. Soc. Annu. Meeting*, Detroit, MI, USA, Oct. 2020, pp. 1–6.

**MD. MINARUL ISLAM** (Member, IEEE) received the B.Sc. and M.Sc. degrees in electrical and electronic engineering from the Bangladesh University of Engineering and Technology, Dhaka, Bangladesh, in 2007 and 2013, respectively, and the Ph.D. degree in electrical engineering from the University of Wollongong, Wollongong, NSW, Australia, in 2022. He was an Exchange Master's Student with the University of Flensburg, Germany, in 2011. He is currently an Assistant Professor with the Department of Electrical and Electronic Engineering, University of Dhaka. His research interests include grid integration of renewable energy sources, power system planning and control, inrush and fault current limiters, renewable energy, solar PV, wind turbines, power grids, and power system stability.

From 2008 to 2009, he was with Huawei Technologies (Bangladesh) Company, Ltd. From 2009 to 2016, he was with Stamford University Bangladesh, Dhaka, and the Shahjalal University of Science and Technology (SUST), Sylhet, Bangladesh. He is a member of the Electrical Energy Society of Australia (EESA).

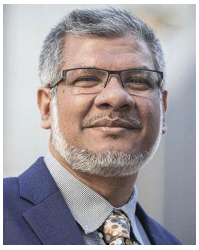

**KASHEM M. MUTTAQI** (Fellow, IEEE) is the Director of the ARC Training Centre in Energy Technologies for Future Grids, sponsored by Australian Government, and several industries and Universities in Australia. He is a Senior Professor and the Discipline Leader - Electrical Engineering at the School of Electrical, Computer and Telecommunications Engineering, University of Wollongong, New South Wales, Australia. He was associated with the University of Tasmania, Hobart, Australia as a Research Fellow/Lecturer/Senior Lecturer from 2002 to 2007, and with the Queensland University of Technology, Brisbane, Australia as a Research Fellow from 2000 to 2002. Previously, he worked for Multimedia University, Selangor, Malaysia as a Lecturer for three years. He received the B.Sc. degree in electrical and electronic engineering from Bangladesh University of Engineering and Technology (BUET), Dhaka, Bangladesh, in 1993, the M.Eng.Sc. degree in electrical engineering from University of Malaya, Kuala Lumpur, Malaysia, in 1996, and the Ph.D. degree in Electrical Engineering from Multimedia University, Selangor, Malaysia in 2001. He has 25 years of academic experience and authored or coauthored 500 papers in international journals and conference proceedings. He is a Fellow of the Institution of Engineers Australia (FIEAust). He is a Fellow of the Institution of Engineering and Technology UK (FIET). He has become a Fellow of the Institute of Electrical and Electronics Engineers (IEEE).

**DANNY SUTANTO** (Life Senior Member, IEEE) received the B.Eng. (Hons.) and Ph.D. degrees in electrical engineering from the University of Western Australia, Perth, WA, Australia, in 1978 and 1981, respectively. He is currently serving as the Professor of power engineering with the University of Wollongong, Wollongong, NSW, Australia. His research interests include power system planning, power system emergency, analysis and harmonics, flexible alternating current transmission systems, and battery energy storage systems. He was the IEEE Industry Applications Society Area Chair for Region 10 (Asia–Pacific) from 2014 to 2017.

**MD. MOKTADIR RAHMAN** received the B.Sc. degree in electrical engineering from the American University of Bangladesh in 2008, the M.Sc. and M.Phil. degrees in power system and renewable energy from City, University of London, U.K., in 2011 and 2015, respectively, and the Ph.D. degree in electrical engineering from Murdoch University, Australia, in 2018. He was a Power System Engineer with OST Energy, U.K., after completing his M.Sc. degree. He held two post-doctoral positions in Australia supported by ARENA and the City of Melville, WA, Australia, after the completion of his Ph.D. degree. He is currently a Senior Power System Engineer with Essential Energy, Australia. He has more than eight years of experience in the power and renewable energy engineering sectors. He was involved in grid connection and modeling of more than 3GW of solar PV and battery project implementations across Australia. He is a partner investigator of the ARC Training Centre in Energy Technologies for Future Grids Project, which is one of the largest ARC-funded (five million AUD) projects in the energy sector of Australia. He has more than eight years of experience in the power and renewable energy engineering sectors. He was involved in grid connection and modeling of more than 3GW of solar PV and battery project implementations across Australia. His research interests include large-scale renewable generator integrations, grid-forming converters, power system stability, and demand side management in distribution networks. He received several competitive awards throughout his academic and industry careers.

**OSCAR ALONSO** received the B.Sc. degree in electrical engineering, the M.Sc. degree in control, electronics and electrical power, and the Ph.D. degree in electrical and electronics engineering from the Public University of Navarre, Spain, in 1994, 1998, and 2008, respectively. He is currently the CEO with SiG coop consulting firm. He has more than 25 years of experience in the research and development of sustainable energy conversion systems, including power converter designing, modeling, testing, and grid integrations. He has also worked as an Engineering Lecturer with the Public University of Navarre, for more than nine years.